Precious and Critical Metal-Bearing Assemblages in the Ann Mason Copper Porphyry Deposit, Yerington, Nevada

Hannah M. Aird*[1], Ceara K. Purcell[1], Nancy DeWitt[1], James Matthews[1], Twyla Capurro[1], Justin Claiborne[1], Jocelyn Bermudez[1], Zachary Meisel[1].

[1]Department of Geological and Environmental Sciences, California State University, Chico, Chico, California 95929, USA.

*Corresponding author email: haird@csuchico.edu; Twitter: @petrologu

This manuscript has been submitted for publication in ORE GEOLOGY REVIEWS. Please note that it is has yet to undergo peer review, and therefore subsequent versions of this manuscript may have slightly different content. If accepted, the final version of this manuscript will be available via the 'Peer-reviewed Publication DOI' link on the right-hand side of this webpage. Please feel free to contact the corresponding author: we welcome any feedback!

Abstract

Porphyry deposits are an important source of copper and their value may be upgraded by minor contents of precious metals, if they are extractable. The mechanisms for enrichment of precious and base metals in these systems are not well understood. This study investigates the deportment of trace metals in the Ann Mason porphyry deposit, including gold, silver, palladium, mercury, lead and bismuth. Petrographic and geochemical data are integrated to characterize the size and habit of minerals, the host mineral assemblages, and their association with alteration assemblages. Ann Mason is one of several ore deposits hosted by the Yerington batholith in Nevada, and is being assessed for copper extraction from bornite and chalcopyrite ore assemblages, associated with potassic alteration. Mineralization assemblages at Ann Mason have been categorized as chalcopyrite-bornite, chalcopyrite-pyrite and pyrite>chalcopyrite zones. Limited two-metre assay data indicates that gold is most closely associated with bornite, although it is found in all three mineralization zones. Analysis by SEM-EDS shows that trace elements are mostly present as microparticles hosted by sulfide minerals. Of the 438 grains measured, 89% are hosted by a sulfide mineral, with 68% hosted by bornite. Silver is most commonly present as hessite and gold as electrum, hosted by bornite and associated with potassic alteration. Palladium, mercury and bismuth are most commonly observed as telluride and selenide minerals. Palladium minerals are associated with potassic alteration, while mercury and bismuth minerals are mostly found with sericitic alteration. High fineness native gold is observed as three round blebs hosted by pyrite or silicates. Observations suggest that the trace metals in the chalcopyrite-bornite zone may have been incorporated by bornite and chalcopyrite, and exsolved upon cooling. In the chalcopyrite-pyrite and pyrite>chalcopyrite zones, the trace metals may have been deposited directly from a mineralizing hydrothermal fluid and incorporated into the growing sulphide minerals. These findings have implications for the paragenesis of porphyry deposits, as well as for the milling processes that would be needed to extract precious metals at the Ann Mason porphyry deposit.

Keywords: Ann Mason; porphyry; gold; silver; sulfides; mineralization.

1. Introduction

Porphyry copper deposits (PCDs) produce around 60% of the world's copper (Johnson et al., 2014) and provide a significant portion of the global supply of gold and tellurium (Goldfarb, 2014), yet the mechanisms of this metal enrichment are still debated. The presence of minor amounts of precious metals such as gold and silver and critical metals such as tellurium, bismuth and the platinum group elements may upgrade the value of the deposit if they are present in a form that is economic to extract (Schulz et al., 2018). Characterization of the trace mineral assemblages that host precious metals, known as geometallurgy, allows a more precise determination of the economic resource; informs industry decisions on the most efficient extraction and processing techniques; and allows for a more complete interpretation of the processes involved in deposition of these mineral assemblages by the mineralizing fluids.

The Ann Mason deposit is a porphyry copper deposit located near Yerington, Nevada. It has a completed preliminary economic assessment and has a combined indicated and measured resource of 1400Mt with a 32% Cu grade, assuming 0.2% Cu cut-off grade (Hudbay Minerals, pers. Comm.). Design of the planned mining and processing operations is underway, making this the ideal time for a geometallurgical study of the precious metal deportment in the Cu-rich ore zones of the deposit. Geometallurgy is an interdisciplinary approach to characterizing the metal resources within a deposit. It combines rock type and characteristics with mineralogy and metal deportment to define different domains of a deposit, which may require different extraction and processing methods to one another. The findings of a geometallurgical study can be used to inform design of the engineering and mineral processing operations for a mine, as well as refine geologic models for ore genesis (Gregory et al., 2013).

Metal deportment describes the distribution, mineral species, textural relationships, grain size and host mineralogy of a given metal within a deposit. Optimization of extraction and processing techniques for a particular deposit depends heavily on the deportment of metals of interest within different domains of the deposit (Agorhom et al., 2013). Precious metals in porphyry deposits may be present as discrete minerals (precious metal sulphides, tellurides, selenides, alloys, etc) or incorporated into the structures of copper sulphides as 'invisible' gold or silver (Arif and Baker, 2004; Harris, 1990), even in much higher-grade ores than those seen at the Ann Mason deposit (Reich et al., 2013). They range in size from <1μm to >100μm, and may be hosted within or at grain boundaries between other minerals, including silicates or sulphides (Agorhom et al., 2013; Arif and Baker, 2004). The size of grains and their location within an assemblage determine the degree of milling required to efficiently extract the metals (Tungpalan et al., 2015), and the speciation and host mineralogy determine the most efficient ore processing techniques in order to optimize metal recovery. The predicted recovery and market value of a precious metal is combined with its distribution and concentrations within the deposit to determine whether it is economic to undertake the extra processing required for extraction of the precious metals in addition to copper. Assay data from the Ann Mason deposit shows elevated gold and silver concentrations generally associated with the bornite-rich region of the deposit, but the metal deportment has never been determined. This study uses petrography, SEM EDS analyses and ICP-MS WDS data to characterize the deportment of silver, gold and palladium bearing microparticles throughout the ore zones of the Ann Mason deposit, to determine the processes of formation and inform industry mineral processing decisions.

2. Geology of the Ann Mason Deposit

The Ann Mason deposit is one of several porphyry and skarn deposits hosted at the edge of the Middle Jurassic Yerington Batholith (169-168Ma; Dilles and Einaudi, 1992). Magmatism in the

region was caused by the Middle Jurassic magmatic arc (170-165Ma) which erupted the subaerial Artesia Lake Volcanics, and emplaced the cogenetic Yerington Batholith; a shallow (~1km) composite intrusion comprising three successive plutons (Dilles, 1987). The McLeod Hill quartz monzodiorite (Jqmd; Carten, 1986; Proffett, 2007) was intruded by the Bear quartz monzonite (Jqm) which was later intruded by the Luhr Hill granite (Jpg). The later stages of the Luhr Hill granite intrusion produced quartz monzodiorite porphyry (Jqmdp) dykes, which are spatially associated with the majority of the copper mineralization. The Middle Jurassic rocks are unconformably overlain by Oligocene silicic ignimbrites and Miocene andesitic lava flows (Figure 1). The entire sequence of Mesozoic rocks were tilted 90 degrees through Basin and Range faulting, and therefore expose a near-total Jurassic cross section at the surface (Dilles and Einaudi, 1992). This makes the region ideal for studying the conditions of formation of the porphyry and skarn deposits distributed around the edge of the batholith.

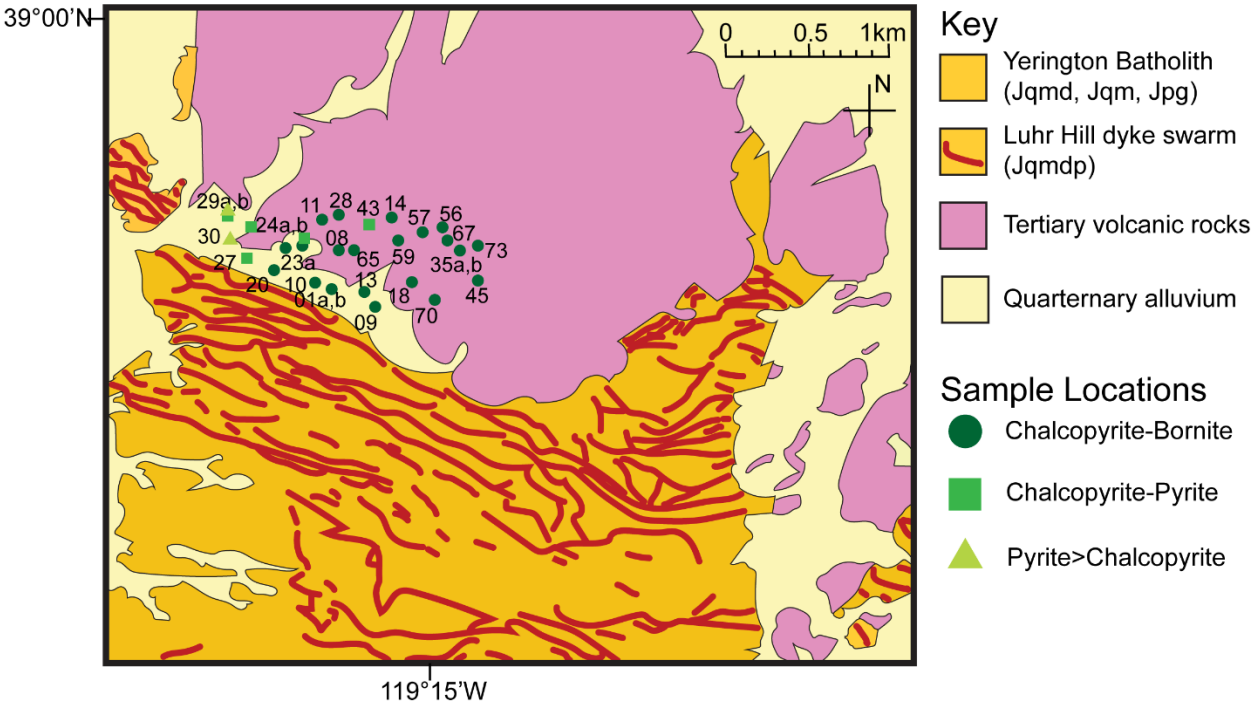

Figure 1: Geologic map of the Ann Mason district, showing sample locations and their mineralization zones. Modified from Proffett and Dilles (1984).

Alteration and Mineralization at Ann Mason:

The Ann Mason Deposit is located on the southern margin of the Yerington Batholith, and comprises zones of altered intrusive rocks at about 2.5-4km paleodepth (Dilles and Einaudi, 1992). Alteration of the primary mineralogy was caused by the interaction of a high-temperature fluid with the host plutonic rocks, and is commonly associated with the deposition of ore minerals. The majority of ore mineralization is centered around the Luhr Hill porphyritic granite (Jpg) and cogenetic granite dyke swarm (Jqmdp), which are believed to be the source of the mineralizing hydrothermal fluid (Dilles and Einaudi, 1992), dating the alteration to 168.5Ma.

Main stage alteration comprised propylitic (albite+epidote+actinolite+chlorite) above 4km paleodepth, sodic-calcic (oligoclase-actinolite-sphene) from 3.5 to >6km, and potassic (biotite+K feldspar) from 1 to 6km (Dilles et al., 1992; Dilles and Einaudi, 1992). Late stage sodic, chloritic and sericitic alteration formed a funnel-shaped zone from 4km paleodepth upwards, and comprised early sodic (albite-chlorite-vermiculite to albite-sericite-pyrite), grading laterally to chloritic alteration (chlorite+sericite).

Copper mineralization is predominantly spatially associated with zones of potassic alteration, with granite porphyry dykes, with quartz veins and saline fluid inclusions (Dilles and Einaudi, 1992). The most important Cu ore minerals are bornite and chalcopyrite, and the mineralized region may be divided into several zones of mineralization: chalcopyrite-bornite (Ccp-Bn), chalcopyrite only (Ccp), chalcopyrite-pyrite (Ccp-Py), pyrite>chalcopyrite (Py>Ccp) and pyrite only (Py). The Ccp-Bn zone is exposed at the greatest paleodepth, grading upwards and outwards through Ccp, Ccp-Py and Py>Ccp to Py at shallower depths and greater paleolateral extents.

Our samples contain potassic alteration overprinted by late stage albite-chlorite and sericite-quartz alteration, and are from the Ccp-Bn, Ccp-Py and Py>Ccp mineralization zones (Figure 1).

3. Methods

Thirty samples were collected from the Hudbay Minerals drillcore repository in Yerington, Nevada. Hudbay Minerals determined, through geochemistry and core logging of more than 800,000m of core from 79 drill holes, that Au and Ag are associated with bornite-enriched zones, which is consistent with the literature (e.g. Arif and Baker, 2004). Samples for this study were therefore selected based on two metre assay data from Hudbay Minerals: two metre sections with the most elevated Au and Ag concentrations were targeted and 10-20cm-long core samples were chosen based on visual inspection of the two metre section. Where possible samples containing visible sulphides were preferentially selected, on the basis of the observed correlation between Au concentrations and bornite content by Hudbay Minerals. A range of samples was also chosen to represent and investigate a variety of host rocks, several alteration assemblages and the three mineralization assemblages (Table 1).

Polished sections were produced and petrographically described using an Olympus BX51 microscope to determine the primary and secondary textures and mineral assemblages. Photomicrographs were taken of notable features of each sample using a Stream Essentials SC30 Camera, documenting key minerals and textures in plane polarized and cross polarized transmitted light and in reflected light. Reflected light microscopy was used to determine the sulphides and other opaques in each sample.

Energy-dispersive spectroscopy (EDS) scans were performed on specific sulphides and other minerals within the samples using a Tescan Vega 3 SEM to determine the chemical composition of the minerals and allow more precise identification. Back-scattered electron (BSE) imaging with a beam current of 7-14 nA was commonly used to find the sulphide assemblages of interest. An acceleration voltage of 10-30 kV was used to reach between 10,000 and 25,000 counts per second

158 at a working distance of 10 microns to establish proper conditions for the EDAX x-ray software to
159 determine chemical assemblages. Spot size was between 90 to 150 nm.
160
161 Representative examples of the main Au-bearing mineral assemblages were analyzed by
162 wavelength-dispersive spectroscopy (WDS) using the electron microprobe (EPMA) at the
163 University of California, Davis to quantitatively determine the compositions of each phase. An
164 accelerating voltage of 15 kV, a beam current of 20 nA and a counting time of 30 s were used.
165
166 The distribution of samples with regard to original lithology, alteration type and mineralization
167 type are listed in Table 1.
168
169 **4. Results**
170 *4.1. Petrography: Alteration*
171 Samples in this study have undergone potassic and subsequent late stage albite-chlorite and
172 sericite-quartz alteration.
173 4.1.1. Potassic Alteration
174 *Potassic alteration* comprises replacement of hornblende by sagenitic biotite, replacement of
175 plagioclase by K feldspar and significant recrystallization of groundmass with fine crystalline,
176 mosaic-textured quartz and fine crystalline secondary biotite. Sagenitic biotite (Figure 2a) contains
177 tiny oriented needles of titanite.
178 4.1.2. Sodic Alteration
179 *Sodic alteration* comprises replacement of biotite by chlorite and sulphides, and sparse formation of
180 epidote. K-feldspar has rims of albite and plagioclase has irregular zoning (Figure 2d, e). Feldspars
181 are pervasively but not intensely sericitized. Titanite is associated with patches of chlorite. Calcite
182 veins crosscut the assemblage, hosting anhedral chalcopyrite (Figure 2b).

183 4.1.3. Sericite-Quartz Alteration

184 *Sericite-quartz alteration* comprises replacement of feldspars by sericite, and may obliterate
185 primary igneous rock texture, resulting in a groundmass of sericite and quartz (Figure 2c, d).
186 Plagioclase is commonly more intensely altered than K feldspar. Medium-crystalline, tabular
187 muscovite may also be observed in patches or veins crosscutting a sericitized groundmass (Figure
188 2f). Fine sericite replaces feldspar phenocrysts, and groundmass is commonly formed of fine
189 sericite and quartz (SQ assemblage from Dilles and Einaudi, 1992). Moderate to intense sericite-
190 quartz alteration is associated with the presence of pyrite in the samples.

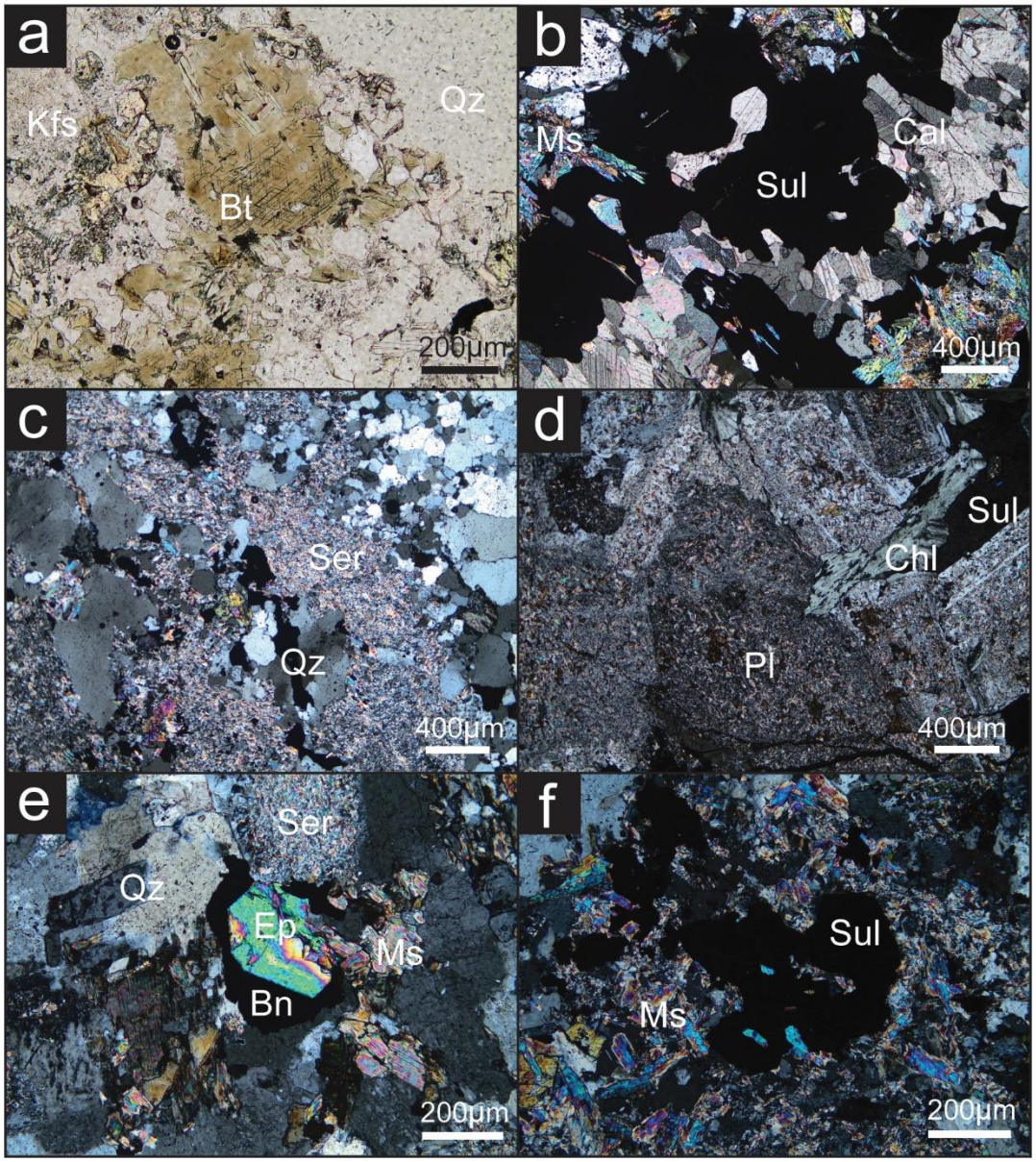

Figure 2: Silicate alteration of the Ann Mason deposit. a) sagenitic biotite in EG-AM-15; b) Calcite and pyrite vein with muscovite in EG-AM-43; c) pervasive sericite alteration cut by quartz veins in EG-AM-27; d) sericitized feldspars with chlorite and sulphide minerals in EG-AM-43; e) bornite and chalcopyrite wrapping around epidote in association with sericite and muscovite in EG-AM-10; f) sulphide minerals with muscovite in EG-AM-27. Abbreviations: Kfs K-feldspar, Bt biotite, Qz quartz, Ms muscovite, Sul sulphide minerals, Cal calcite, Ser sericite, Pl plagioclase, Chl chlorite, Ep epidote, Bn bornite.

4.2. Petrography: Mineralization

Ore mineral assemblages in this study have been categorized by their sulphide mineralogy, on the basis of Dilles and Einaudi (1992).

4.2.1. Chalcopyrite-Bornite Zone (Ccp-Bn)

Sulphides in the Ccp-Bn zone are commonly multiphase (bornite and chalcopyrite), sub- to anhedral and hosted within quartz-rich veins. Sulphides rarely enclose quartz or epidote crystals (Figure 3d). Sulphides may also be associated with secondary biotite within quartz veins. Chalcopyrite textures vary from comprising the majority of a multiphase sulphide to lamellae in a predominantly bornite crystal (Figure 3a-d), and many of the dominantly chalcopyrite crystals have heavily pitted surfaces. Some multiphase sulphides include areas of tennantite on the edge of bornite (Figure 3b).

4.2.2. Chalcopyrite-Pyrite Zone (Ccp-Py)

Sulphides are dominantly anhedral chalcopyrite, typically as small crystals with pitted surfaces. Chalcopyrite is commonly disseminated through the groundmass, but may be hosted within quartz or calcite veins. Conversely, pyrite crystals are subhedral with smooth surfaces, and may contain small rounded inclusions of chalcopyrite, or be surrounded by interstitial chalcopyrite (Figure 3f). Pyrite is commonly but not exclusively associated with patches of medium crystalline muscovite. Bornite is very rare, but when present is closely associated with chalcopyrite, and has a similarly anhedral shape and pitted surface.

4.2.3. Pyrite>Chalcopyrite Zone (Py>Ccp)

Pyrite is the dominant sulphide, is typically subhedral, with smooth surfaces and is concentrated in veins of medium crystalline, mosaic textured quartz. Subordinate chalcopyrite is anhedral with a pitted surface and is interstitial to pyrite, contained within pyrite, or as discrete crystals (Figure 3e). Bornite is very rare, but where present is closely associated with chalcopyrite. Chalcopyrite commonly forms rims around pyrite crystals.

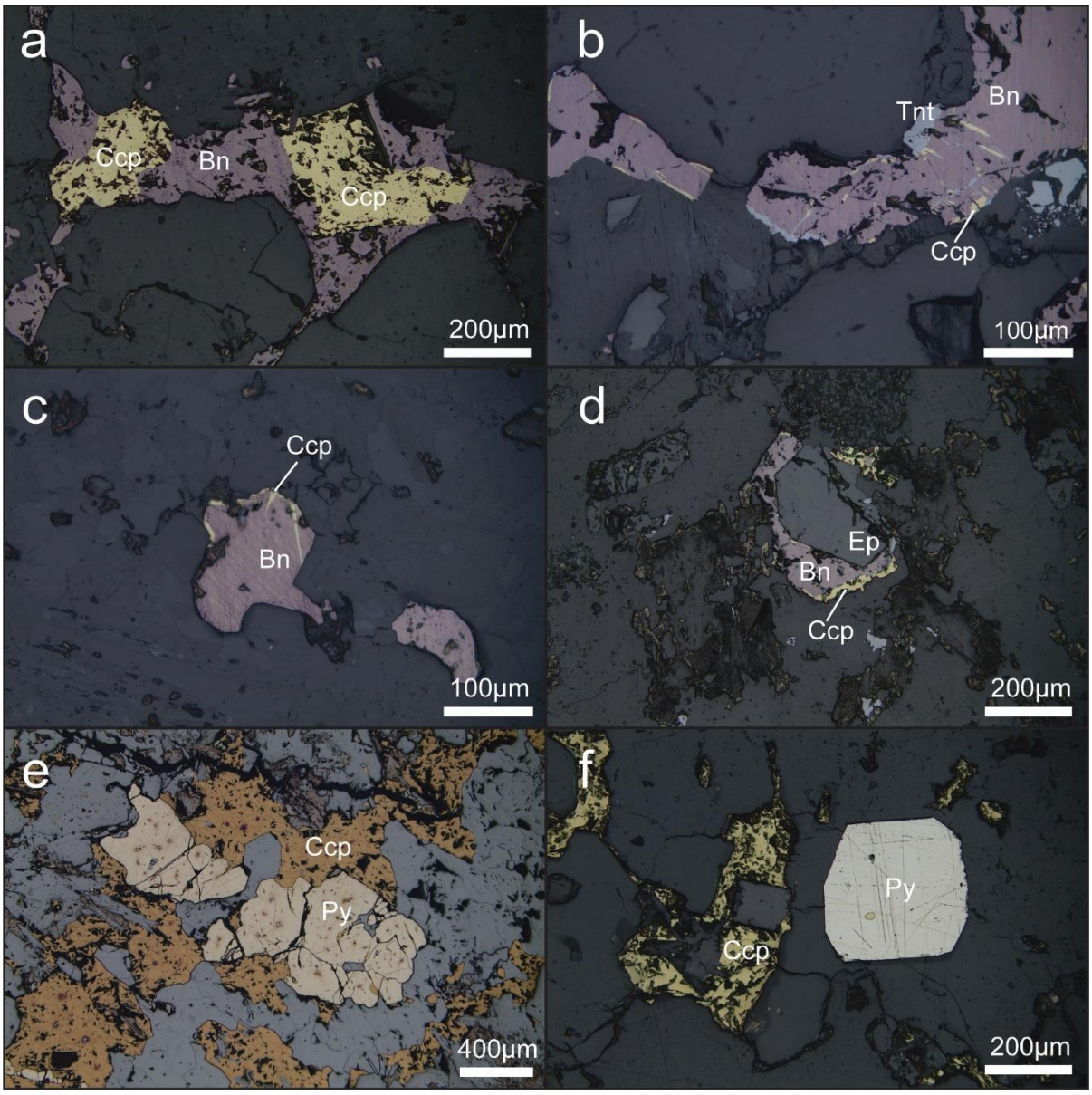

Figure 3: Sulphide mineralization of the Ann Mason deposit. a) bornite surrounding chalcopyrite in EG-AM-01a in the Ccp-Bn zone; b and c) chalcopyrite lamellae in bornite edged by tennantite in EG-AM-08 in the Ccp-Bn zone; d) bornite edged by chalcopyrite surrounding epidote in EG-AM-10 in the Ccp-Bn zone; e) chalcopyrite interstitial to pyrite containing chalcopyrite inclusions in EG-AM-43 in the Ccp-Py zone; f) chalcopyrite near euhedral pyrite containing a chalcopyrite inclusion in EG-AM-27 in the Ccp-Py zone. Abbreviations: Ccp chalcopyrite, Bn bornite, Tnt tennantite, Ep epidote, Py pyrite.

238 *4.3. Precious Metal Deportment*

239 Thirty samples were analysed in this study, yielding a total of 438 individual precious metal
240 minerals (PMM).

241 A total of 90 gold-bearing grains (in 29 samples) and 389 silver-bearing grains (in 30 samples)
242 were analysed (Figure 4). Gold is hosted predominantly in the form of electrum, with subordinate
243 occurrences of Au-Ag telluride and native gold. The majority of silver is hosted as silver telluride
244 minerals (most commonly hessite, but also Au-Ag, Pd-Ag or Ag-Bi tellurides), with subordinate
245 electrum and silver selenides. Ten occurrences of Pd minerals were observed in six samples, 29
246 occurrences of Bi minerals in six samples, and six occurrences of Hg minerals in three samples.

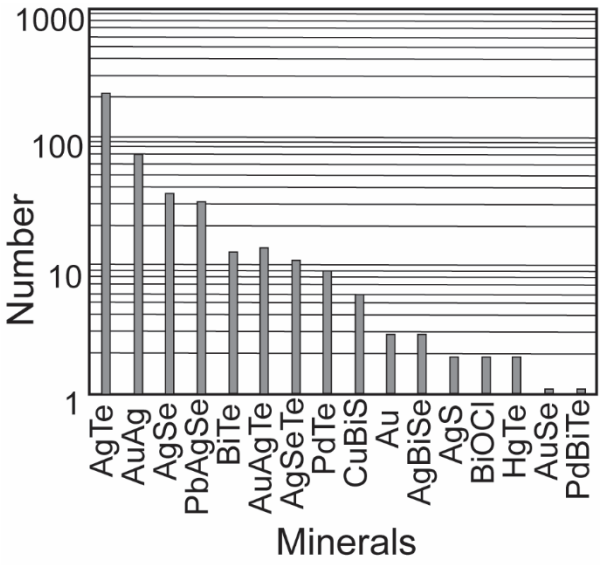

247

248 **Figure 4**: Frequency of microparticle mineral analyses observed.

249

250 Precious metal-bearing mineral species were mostly associated with sulphide minerals, either
251 within or on the edge of sulphide grains, or as isolated grains hosted within silicate minerals. From
252 a total of 438 precious metal-bearing minerals analysed, 89% were associated with either bornite,
253 chalcopyrite or pyrite, with 68% associated with bornite, 16% associated with chalcopyrite, 6%
254 associated with pyrite and 2% associated with tennantite, while 9% were hosted as 'free' grains
255 isolated within silicate minerals (Figure 5), including potassium feldspar and quartz. Almost all

256 microparticles are located along the edges of sulphides, along fractures or with microporosity
257 within sulphides.

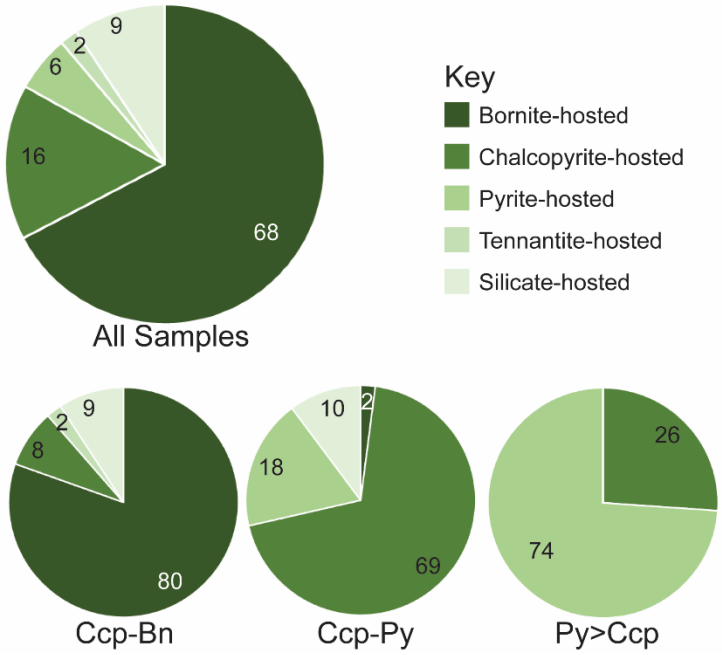

258

259 **Figure 5**: Proportion of microparticles hosted within bornite, chalcopyrite, pyrite, tennantite and
260 silicate minerals in all samples; in the Ccp-Bn zone; in the Ccp-Py zone; and in the Py>Ccp zone.

261

262 Within the Ccp-Bn zone, 80% of precious metal minerals are hosted within or on the edge of
263 bornite, 8% are hosted by chalcopyrite, 2% by tennantite and 9% by silicate minerals. In the Ccp-Py
264 zone, 69% are hosted by chalcopyrite, 2% by bornite, 18% by pyrite and 10% by silicates. In the
265 Py>Ccp zone, 26% are hosted by chalcopyrite and 74% by pyrite (Figure 5).
266 Precious metal deportment is consistent across all original rock lithologies, confirming that the
267 composition of the pre-mineralization rock is immaterial to the final precious metal mineral
268 assemblage.
269 The occurrence and characteristics of different precious metal minerals are summarized in Table 2
270 and described individually below. This research was carried out through semi-quantitative SEM
271 analysis, so only tentative mineral identifications have been made. In some cases further EPMA

analyses would be required to distinguish between several mineral options, but the majority of the particles were too small to accurately determine composition.

4.3.1. Electrum and native gold

Native gold and native silver are defined on a compositional continuum, with native gold comprising $Ag_{0-0.65}Au_{1-0.35}$ and native silver comprising $Ag_{0.65-1}Au_{0.35-0}$ (Palyanova, 2020). Due to the qualitative nature of our analysis, in this study we have classed microparticles containing solely Au as *native gold*, and microparticles containing even a little silver as *electrum*. By this definition, we have only observed three microparticles of native gold, but really we have only observed three microparticles of *high fineness* native gold, and much of the observed 'electrum' should likely be reclassified as native gold of lower fineness.

Electrum is predominantly observed in the Ccp-Bn zone, with 69 of the 72 electrum occurrences in this zone. Electrum is generally globular in shape and ranges in size from 1-13.5μm. It is most commonly hosted within bornite (Figure 6a, c, e).

Native gold: three grains are observed in the samples analyzed. All are associated with sericitic alteration, and are present as round blebs. In the Py>Ccp zone, native gold (n=2; 3.4 and 9.4μm diameter) is hosted within pyrite which is associated with muscovite, mosaic quartz, sericitized K-feldspar and chlorite (Figure 7 c, h). In the Ccp-Bn zone, native gold (n=1; 6.4 μm) is hosted within secondary K-feldspar and mosaic quartz.

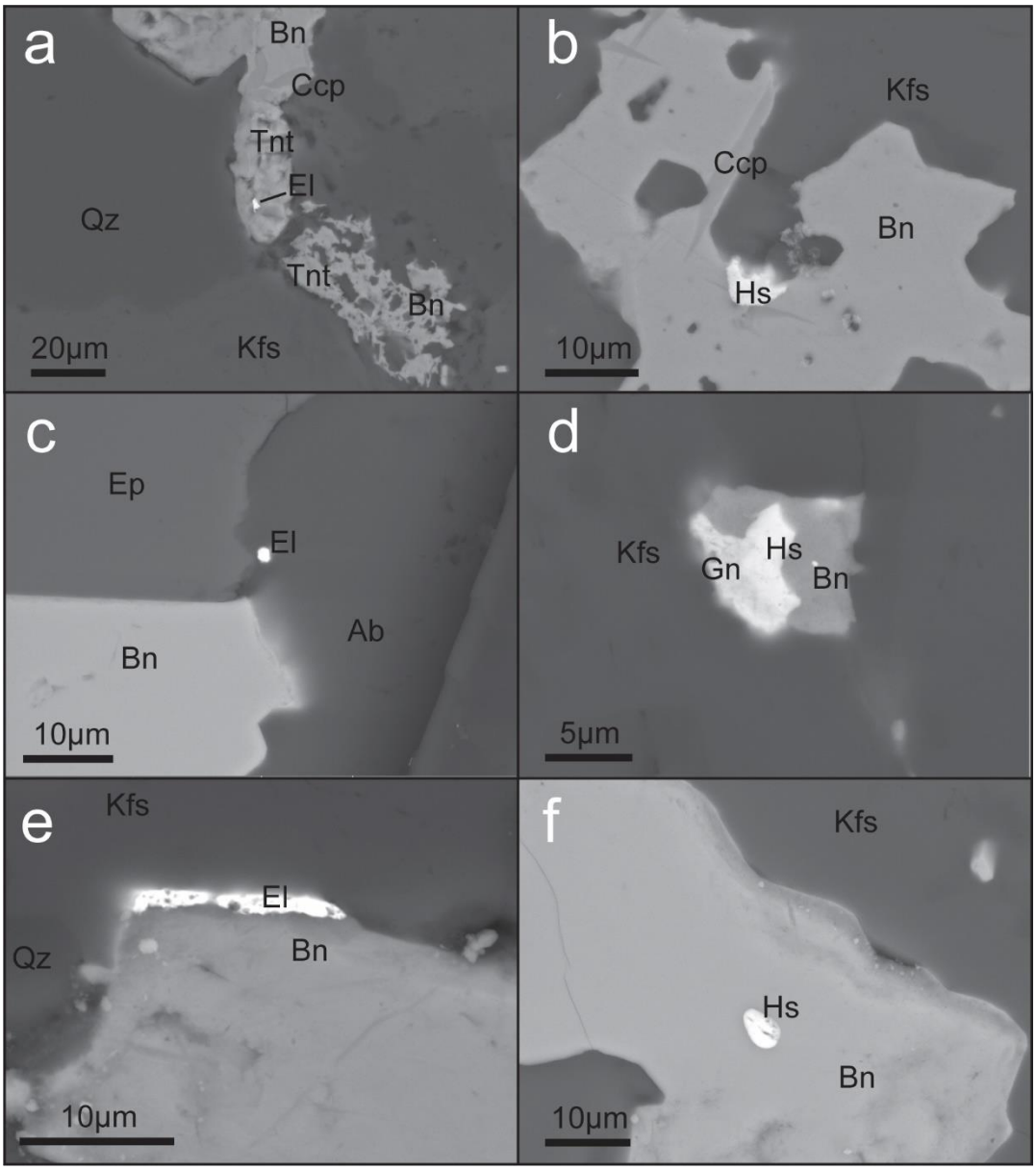

Figure 6: Representative photomicrographs of hessite and electrum in the Ann Mason deposit. a) electrum hosted by tennantite in EG-AM-35b; b) hessite hosted by bornite with chalcopyrite lamellae in EG-AM-35b; c) electrum hosted by albite and epidote near bornite in EG-AM-57; d) multiphase particle of hessite and galena hosted by bornite within K-feldspar in EG-AM-35b; e) electrum on the edge of bornite and K-feldspar in EG-AM-57; f) hessite in bornite in EG-AM-57. Abbreviations: Bn bornite, Ccp chalcopyrite, Tnt tennantite, Gn galena, El electrum, Hs hessite, Qz quartz, Kfs K-feldspar, Ep epidote, Ab albite.

4.3.2. Telluride Minerals

Telluride minerals are most prevalent in the Ccp-Bn zone, especially hessite (Ag_2Te), with 210 of the 216 hessite occurrences being observed in the Ccp-Bn zone. Over 85% of the hessite present in the Ccp-Bn zone is hosted by bornite: 36% on the edges of crystals, and 49% within crystals. In the Ccp-Bn zone, only 7% are associated with chalcopyrite crystals, and 9% are hosted as isolated grains within silicate minerals including plagioclase, biotite and potassium feldspar. When present within a sulphide crystal, hessite commonly has either an acicular or a rounded habit, and grains range in size from 0.5 to 27.2µm (Figure 6 b, d, f). Based on the results of EPMA analysis (see Supplementary Data) the contents of Ag and Te in hessite are 64.114 atomic % and 35.886 atomic % respectively. This gives a composition of $Ag_{1.8}Te$, which has a slightly higher ratio of Te to Ag than stoichiometric proportions of Ag_2Te. Hessite is observed in composite microparticles with Au-Ag-Te (Ccp-Bn, Figure 7l) and with Bi-Te (Py>Ccp, Figure 7g).

Au-Ag-Te (possibly sylvanite, $(Au,Ag)_2Te_4$; muthmannite, $AuAgTe_2$; krennerite, Au_3AgTe_8; or petzite, Ag_3AuTe_2) shows a similar distribution to hessite within the Ccp-Bn zone (n = 11). Grains range in size from 0.7 to 10.7µm (Figure 7k, l).

Pd- and Pd-Bi-bearing telluride species are only present in the Ccp-Bn zone, predominantly hosted within or on the edge of bornite or tennantite, likely as merenskyite ($(Pd,Pt)(Bi,Te)_2$). Merenskyite crystals (n=9) range in size from 1 – 10.8µm (Figure 7i). Only one Bi-bearing merenskyite grain was observed, measuring 3µm and hosted in bornite. Merenskyite was observed in a composite microparticle with clausthalite (PbSe)in the Ccp-Bn zone (Figure 7j).

Bi-Te (further analysis required to determine mineral name, but this was outside the scope of this study) ranges in size from 1.7-18µm (n=13) and is hosted within or on the edge of pyrite crystals, located within the Py>Ccp zone (Figure 7b, d, e, g). It is also observed (n=4) isolated within silicates in the Ccp-Bn zone. Bi-Te is only observed in samples where native gold is also present.

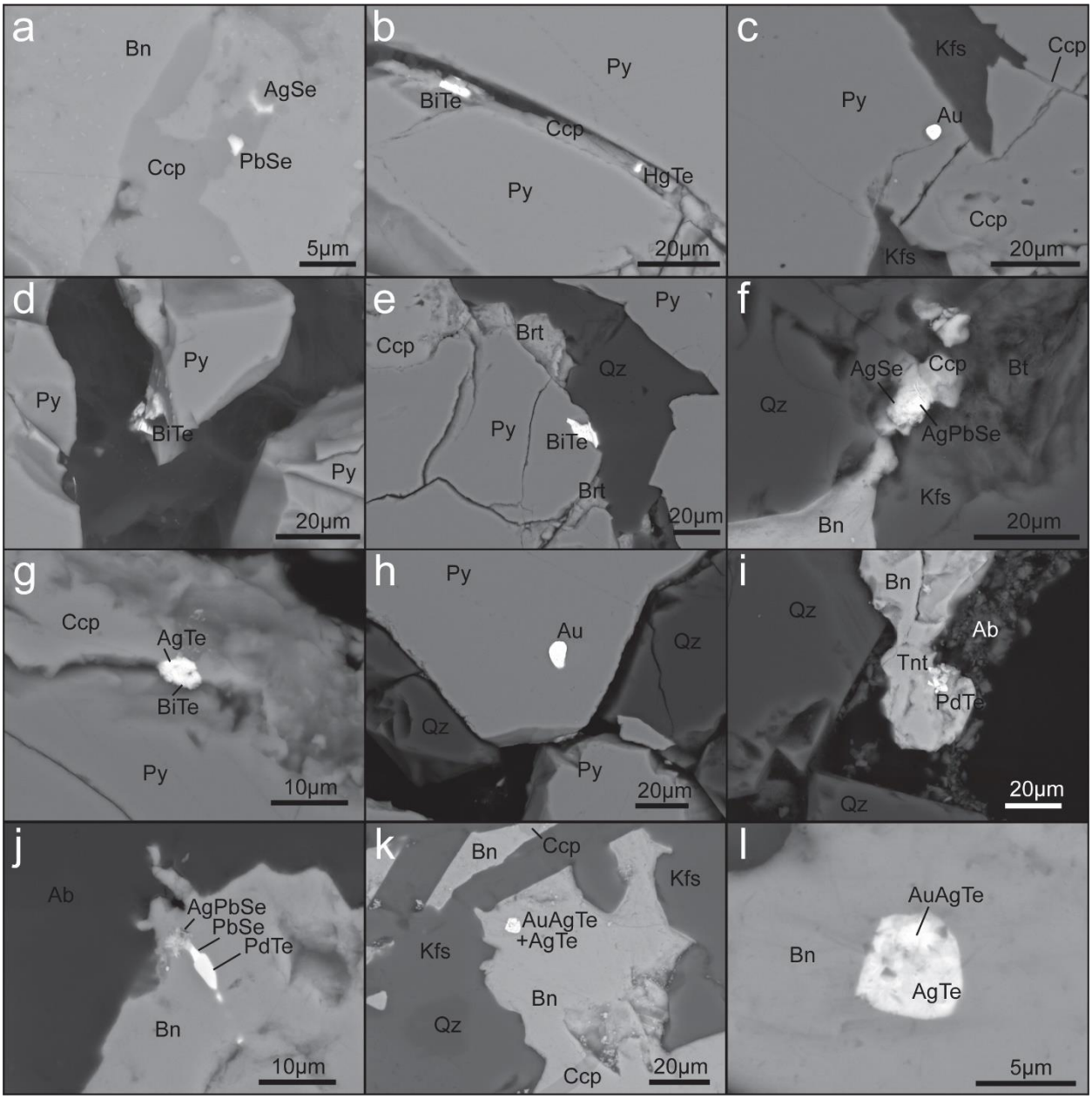

Figure 7: Representative photomicrographs of microparticles in the Ann Mason deposit. a) PbSe and AgSe in chalcopyrite within bornite in EG-AM-73; b) Hg- and Bi- tellurides in chalcopyrite filling a fracture through pyrite in EG-AM-30; c) Native gold in pyrite cut with chalcopyrite-filled fractures in EG-AM-30; d) Bi-telluride on the edge of pyrite in EG-AM-30; e) Bi-telluride in the edge of pyrite associated with baryte, chalcopyrite and quartz in EG-AM-30; f) Multiphase particle of AgSe and AgPbSe between chalcopyrite and bornite associated with biotite in EG-AM-35a; g) Multiphase particle of hessite and Bi-telluride between bornite and chalcopyrite in EG-AM-30; h) Native gold in pyrite in EG-AM-30; i) Merenskyite in tennantite on the edge of bornite in EG-AM-35a; j) Multiphase particle of merenskyite, clausthalite (PbSe) and AgPbSe in bornite in EG-AM-35a; k, l) Multiphase particle of AuAgTe and hessite in bornite with chalcopyrite lamellae in EG-AM-57. Abbreviations: Bn bornite, Ccp chalcopyrite, Py pyrite, Kfs K-feldspar, Brt baryte, Qz quartz, Bt biotite, Ab albite.

Hg-bearing telluride species (likely Coloradoite HgTe) is 2.4-6.7μm (n=2) and is hosted within chalcopyrite filling a fracture through pyrite (Figure 7b) or within silicates close to a sulphide crystal. This mineral is only observed within the Ccp-Py or the Py>Ccp zones. Hg-Te is observed in composite microparticles with Bi-Te in the Py>Ccp zone.

4.3.3. Selenide Minerals

Selenide minerals are 3.5 times more prevalent in the Ccp-Py zone (n=33 in 3 samples) than in the Ccp-Bn zone (n=37 in 12 samples), although the former is dominated by Ag-Se and the latter by Pb-Ag-Se crystals.

Ag-Se (likely naumannite, Ag_2Se) ranges in size from 1-14.8μm (n=37) and are dominantly located on the edge of chalcopyrite (Figure 7a, f). Of all the Ag-Se observed, 27% were found in the Ccp-Bn zone and the remaining 73% were in the Ccp-Py zone.

Pb-Ag-Se (composition does not match any known mineral, but likely naumannite with Pb substitution for Ag) ranges in size from 1-8μm (n=31) and are located almost entirely on the edge of bornite crystals (Figure 7f, j). Of the Pb-Ag-Se minerals, 16% were in the Ccp-Py zone and the remainder were in the Ccp-Bn zone.

Ag-Te-Se (likely kurilite, Ag_8Te_3Se) are mostly associated on or within chalcopyrite within the Ccp-Py zone. Crystals range from 2.1-7.6μm (n=10).

Au-Se: only one AuSe crystal (4.3μm) was observed in the Ccp-Py zone isolated in silicates (composition does not match any named mineral).

Ag-Bi-Se (possibly bohdanowiczite $AgBiSe_2$) was observed in the Ccp-Bn zone, ranging in size from 4.7 to 1.2μm (n=3) and hosted by chalcopyrite.

Clausthalite (PbSe) was commonly observed throughout the Ccp-Bn zone, but was not specifically recorded and measured in this study (Figure 7a, j).

4.3.4. Other Minerals

Two occurrences of acanthite (Ag_2S) were observed in the Ccp-Py and Py>Ccp zones. Crystals ranged in size from 3-4.7μm and were associated with chalcopyrite.

Bi-bearing copper sulphides (likely Wittichenite Cu_3BiS_3) are observed in the Ccp-Bn zone(n=6), associated with bornite (n=5) and ranging in size from 26.4-5.5μm. One 2μm crystal is hosted within chalcopyrite.

Bismoclite (BiOCl) ranges in size from 3.8 - 4μm and is observed isolated in silicates within two samples from the Ccp-Py zone.

5. Discussion

5.1. Mineralization and Alteration

Previous research has described the association of Cu-sulfide bearing assemblages with potassic alteration (Dilles and Einaudi, 1992). Our petrographic results support the association of the chalcopyrite-bornite assemblage with potassic alteration, and find that the majority of precious metal microparticles are also hosted by bornite within this assemblage, as also seen at Elatsite and Assarel deposits in Bulgaria (Cioacă et al., 2020).

5.1.1 Formation of Ccp-Bn Assemblages:

Textural relations suggest that chalcopyrite was the first mineral to precipitate from the hydrothermal fluid that produced potassic alteration, and that bornite likely formed through continued reaction of chalcopyrite with fluids (Figure 8a, b). Experimental data show that chalcopyrite may be replaced by *bdss* (bornite-digenite solid solution) through reaction with solutions containing Cu-chloride complexes and hydrosulfide, between ~200-320°C (Zhao et al., 2014). The composition of the *bdss* depends on the reaction temperature, with a higher proportion of bornite at higher temperature ($Bn_{93}Dg_7$ at 320°C; (Zhao et al., 2014). Replacement occurs at the boundaries of chalcopyrite and proceeds inwards towards the crystal core (e.g. Figure 3a), producing textures similar to those seen in the ccp-bn mineralization zone at Ann Mason (e.g. Li et

al., 2020, 2018; Zhao et al., 2014), showing a sharp reaction front between a chalcopyrite core rimmed by bornite. These textures suggest that the dissolution of chalcopyrite is accompanied by the precipitation of bornite through interface coupled dissolution reprecipitation (ICDR) reactions, facilitated by micropores within the sulphide crystals. If Fe was only sparingly soluble in the mineralizing fluid, pseudomorphic replacement may also have been accompanied by overgrowth of bornite on the outside of the original chalcopyrite crystal (Li et al., 2020).

Bornite forms from *bdss* through recrystallization (Zhao et al., 2014), which also allows annealing of micropores in the bornite crystal structure. As annealing occurs, the bornite may exsolve chalcopyrite lamellae, as seen in Figure 3b and c. The formation of these lamellae is a fluid-mediated reaction, likely driven by either loss of Cu to or addition of S from the fluid (Li et al., 2018).

5.1.2. Formation of Ccp-Py and Py>Ccp Assemblages:

As the Ccp-Py and Py>Ccp assemblages only appear to differ in their proportions of pyrite and chalcopyrite (possibly due to the small number of samples from these zones), they will be discussed together. Both assemblages are associated with moderate to intense sericitic alteration. In the intensely sericitized samples primary igneous texture is mostly obliterated and the groundmass replaced by fine crystalline quartz and sericite. Pyrite is also commonly in association with fine muscovite crystals in some samples, but there is no clear correlation between proportion of pyrite and intensity of sericitization.

Dilles and Einaudi (1992) noted that the relatively sparse chalcopyrite+pyrite assemblage observed in sodic rocks contrasts with the abundant chalcopyrite+bornite assemblage observed in potassic rocks, and suggested that sodic alteration may have caused Cu-loss. Our data are consistent with Cu-loss from the Ccp-Py and Py>Ccp zones, as chalcopyrite is observed as fine disseminated crystals throughout the groundmass in both the Ccp-Py and the Py>Ccp zones, whereas in the Ccp-Bn zone it is more commonly observed as coarser crystals in quartz veins. Chalcopyrite is also commonly

present in the Ccp-Py and Py>Ccp zones as small inclusions of chalcopyrite within pyrite crystals and as coarser, anhedral chalcopyrite surrounding subhedral pyrite.

Pyrite is present in the Ccp-Py and the Py>Ccp zones as subhedral crystals with a smooth surface, commonly associated with fine muscovite. This texture could be interpreted as precipitation of subhedral pyrite (e.g. Graham and Ohmoto, 1994) from the sericitizing fluid (e.g. Figure 9a). Experimental studies by Blundy et al. (2015) show the precipitation of sulphides directly from a hydrothermal brine, triggered by mixing with a S-rich vapor released by a mafic magma at depth. This process produces significant acid, which would be able to hydrolyze feldspars, producing sericitic alteration. Sericitic alteration has been shown at other deposits to leach chalcopyrite (e.g. Brimhall, 1979). Pyrite can be precipitated in a Cu-enriched environment, and if more Cu is available than can be incorporated into the pyrite structure by solid solution, it precipitates as microparticles and is engulfed by the growing pyrite (Reich et al., 2013). This could explain the small inclusions of chalcopyrite within pyrite crystals in the Py>Ccp and Ccp-Py zones (Figure 9). A later Cu-introduction event could then have formed chalcopyrite after pyrite precipitation (e.g. Gregory et al., 2013). This is not unreasonable given the protracted evolution of porphyry systems through multiple injections of magma (Korges et al., 2020) and thus a constant stream of hydromagmatic fluids. Steadman et al. (2021) suggest that the majority of Cu in porphyry deposits is introduced after pyrite precipitation, as evidenced by fractured pyrite and replacement of pyrite by chalcopyrite containing Au-bearing inclusions. We see evidence of chalcopyrite filling fractures in pyrite in the Ccp-Py and Py>Ccp zones (Figure 7b and c).

5.2. Precious and critical metal mineralization at Ann Mason and comparison with other porphyry deposits

This study shows that the precious and critical metals in the Ann Mason deposit are mostly present as microparticles (<1 - 10μm) of electrum or Au-Ag telluride and selenide minerals, hosted by bornite in the Ccp-Bn mineralization zone.

Gold and silver are the most commonly analysed trace elements of interest in the literature on copper porphyry deposits. Gold is most commonly observed as 5-100um particles of native, or high-fineness gold (<10% Ag content) hosted within or at the edge of copper sulphides such as bornite and chalcopyrite (e.g. Batu Hijau, Red Chris, Kingking, Pebble, Bingham, Grasberg; Arif and Baker, 2004; Gregory et al., 2013; Rees et al., 2015; Rubin and Kyle, 1997; Suerte et al., 2007). More rarely, gold is hosted in pyrite (e.g. Assarel deposit; Cioacă et al., 2020) or by silicate minerals as 'free gold'. In some deposits, including the Red Chris, Granisle and Bell deposits, Au and Ag are predominantly present as electrum (>10% Ag), mostly hosted on the edge of bornite crystals (Cuddy and Kesler, 1982; Rees et al., 2015). Deposits such as Batu Hijau also contain invisible gold and silver held within the crystal structure of bornite, chalcopyrite or pyrite (Arif and Baker, 2004). Other minor forms of gold, silver and bismuth, such as tellurides and selenides, are reported at deposits such as Assarel, Rio Blanco, Santo Tomas II and Bingham (Ballantyne et al., 1998; Cioacă et al., 2020; Crespo et al., 2018; Tarkian and Koopmann, 1995). Deposits such as Santo Tomas II show relatively high concentrations of PGE, primarily held as PGM including merenskyite, kotulskite and moncheite (Tarkian and Koopmann, 1995).

At Ann Mason, microparticles in the Ccp-Bn zone mostly comprise tellurides and electrum, with subordinate Ag-selenides. The most prevalent by far is hessite (58% of all microparticles in Ccp-Bn). The majority of microparticles in the Ccp-Bn zone are hosted by bornite. In the Ccp-Py zone microparticles mostly comprise selenides, especially naumannite (Ag_2Se) and kurilite (Ag_8Te_3Se). Naumannite may be Pb-bearing, but this is more common in the Ccp-Bn zone. The majority of microparticles in the Ccp-Py zone are hosted by chalcopyrite, with some hosted by pyrite, and a few isolated within silicates. The majority of microparticles hosted by chalcopyrite are found on the edge of the chalcopyrite. Microparticles containing Bi and Hg are more common in the Py>Ccp zone, as well as native gold. The majority of microparticles in the Py>Ccp zone are hosted by pyrite, with a few hosted by chalcopyrite, but none is hosted within silicates.

462 *5.3. Formation of precious and critical metal microparticles*

463 There are several possible mechanisms to explain the deportment of precious and critical metals
464 throughout the Ann Mason deposit, including exsolution and precipitation directly from a fluid.

465 5.3.1. Exsolution

466 The distribution of metals between sulphides in the Ccp-Bn zone can most simply be explained by
467 exsolution. Based on a compilation of data from various porphyry deposits by Kesler et al., (2002),
468 Au is most abundantly found in solid solution in bornite, although it may also be present in
469 chalcopyrite up to a few ppm (commonly ppb; George et al., 2018). In our samples the majority of
470 electrum (Ag-Au) and hessite (Ag_2Te) are observed in bornite.

471 Bornite formed by the alteration of chalcopyrite through interaction with hydrothermal fluids, and
472 partitioned other chalcophile elements (Au, Ag, Se, Te) from the fluids into its crystal structure as it
473 grew (Kesler et al., 2002; Simon et al., 2000). Fluid inclusion studies from the Ann Mason deposit
474 suggest that the Cu-bearing assemblages formed between 170 – 550°C (Dilles and Einaudi, 1992),
475 and the lack of digenite lamellae in the bornite suggest that the bornite was formed >320°C (Zhao et
476 al., 2014). Experimental and observational studies indicate that at >350°C, bornite can contain 10s
477 to 100s ppm of Au (Simon et al., 2000), >649ppm of Ag (Reich et al., 2013), >10wt% of Bi (at 300°C;
478 Sugaki et al., 1984), >2000ppm of Se and >400ppm of Te (Cook et al., 2011). The concentration of
479 each element that can be held in solution is temperature-dependent: for example, Au decreases
480 from 1280-8200ppm at 600°C to 235-364ppm at 500°C to 13-80ppm at 400°C (Simon et al., 2000).
481 During cooling, bornite undergoes recrystallization to a crystal structure that is more stable at
482 cooler temperatures (Li et al., 2018; Zhao et al., 2017), but that is able to host lower concentrations
483 of trace elements in solid solution (Simon et al., 2000), causing precious metals to exsolve as
484 discrete minerals. Cook et al. (2011) found that both Se and Te are not especially compatible in
485 bornite, and tend to exsolve as discrete microparticles. The process of exsolution may be facilitated
486 and accelerated by interaction with fluids in the nanopores within bornite (Zhao et al., 2017).

The prevalence in the Ccp-Bn zone of hessite and electrum associated with bornite is consistent with exsolution of these minerals from solid solution (Figure 8c). The majority of these hessite and electrum microparticles are located either at the edge of bornite, or along fractures or apparent porosity within bornite. This distribution is explicable through fluid-driven exsolution, but could also be caused by precipitation directly from a fluid. Alternatively, exsolution of the microparticles may have caused fracturing in the host sulphide, similar to that observed by the replacement of pyrite by chalcopyrite (Zhang et al., 2020).

Another potential mechanism for the formation of hessite and electrum in bornite could be through coupled dissolution-reprecipitation processes, as experimentally demonstrated by Zhao and Pring (2019). If the first microparticles to exsolve from the bornite were Au-tellurides or Au-Ag-tellurides, Te could have been lost through interaction with a hydrothermal fluid, resulting in electrum and hessite. However, direct exsolution of hessite and electrum from the cooling bornite is a simpler explanation for the observed microparticles.

Chalcopyrite is able to host a wide variety of trace elements, though typically in low concentrations unless not associated with another Cu- or Cu-Fe-sulphide (George et al., 2018). For example, when chalcopyrite coexists with bornite, the bornite will contain significantly higher Ag and Bi contents than the chalcopyrite (Cook et al., 2016, 2011). George et al., (2018) suggest that Ag likely substitutes for Cu, while Se and Te are hosted in the S site. Observational studies show that chalcopyrite may contain up to 849ppm Se, up to 1.9ppm Te, >1000ppm Ag and 0.24 ppm Au, 30ppm Bi in solid solution (George et al., 2018). These concentrations are likely temperature-dependent: experimental data show that the concentration of Au in solid solution decreases with temperature from 100-125ppm at 600°C, to 5-80ppm at 500°C to 2-4 ppm at 400°C (Simon et al., 2000).

The reduced capacity of chalcopyrite in the presence of bornite to partition trace elements is reflected in our data, with only 5-6% of hessite and electrum microparticles in the Ccp-Bn zone

512 hosted by chalcopyrite. The majority of microparticles in the Ccp-Py zone are naumannite (Ag_2Se)
513 hosted by chalcopyrite, which is consistent with chalcopyrite containing an order of magnitude
514 more Se than Te in solid solution (George et al., 2018; Reich et al., 2020). Se is also susceptible to
515 fluid-rock interaction (Cook et al., 2011), so naumannite in the Ccp-Py zone may contain Se that has
516 been remobilized and redeposited by fluids.
517 Experimental studies suggest pyrite may contain 240ppm and 300ppm Au and Ag respectively,
518 contained within solid solution or as micro inclusions (Pal'Yanova et al., 2015), which is
519 significantly more than may be incorporated into chalcopyrite. However, in the Ccp-Py zone 72% of
520 Ag- and Au-bearing particles are hosted by chalcopyrite and only 19% by pyrite, while most
521 microparticles in the Py>Ccp zone comprise Bi- or Hg-bearing minerals hosted by pyrite. The
522 paucity of Au and Ag-bearing particles in pyrite suggests that the pyrite may have formed from a
523 fluid relatively depleted in Au and Ag, and that the pyrite and chalcopyrite in these zones may have
524 formed from different fluid events. Deditius et al. (2011) suggested that nanoparticles in pyrite may
525 form either by exsolution or by direct precipitation from a fluid. The occurrence of high fineness
526 native gold and of Bi-tellurides only in pyrite or isolated in silicates, suggest that direct
527 precipitation from a fluid is the more likely mechanism for these minerals (as discussed in more
528 detail below). This interpretation is supported by the two-dimensional areal proportions of one of
529 the native gold microparticles (60μm^2) and its host pyrite (49,390μm^2), giving a 2D proportion of
530 1,215ppm Au in the pyrite, which is too much Au to have been originally held in the pyrite crystal
531 structure.
532 5.3.2. Direct precipitation from a fluid
533 It is also possible that microparticles could have been precipitated directly from a fluid (e.g.
534 Deditius et al. 2011), as seems the most likely explanation for microparticles hosted by pyrite and
535 chalcopyrite in the Ccp-Py and Py>Ccp zones. Studies have shown that gold and silver minerals may
536 precipitate even if the component elements are not saturated within the fluid (Gammons and

Williams-Jones, 1997, 1995; Gregory et al., 2013; Kesler et al., 2002; Pokrovski et al., 2008; Simon et al., 2000; Williams-Jones and Heinrich, 2005), and these hydrothermal fluids could have directly precipitated nanoparticles of Au- and Ag-bearing minerals in the nanopores during sulfide formation. Nanoparticles form from fluids when nucleation rates are much faster than growth rates (e.g. Hochella et al., 2008; Zhou et al., 2021). The nanoparticles could have coarsened through Ostwald ripening (Deditius et al., 2011; Ruiz-Agudo et al., 2014), and become trapped in the sulfide as the nanopores annealed.

Although common in epithermal environments, precious metal-bearing selenides and tellurides are rare in porphyry environments, leading Plotinskaya et al. (2018) to suggest that these minerals formed through interaction of the sulphides through a late epithermal fluid. The concentration of the microparticles at the edges of or along fractures within the sulphides would be consistent with this interpretation. Fluid inclusion studies suggest that the late sodic alteration was caused by fluids at ~100-250°C (Dilles and Einaudi, 1992), which is consistent with epithermal formation temperatures. This likely explains the formation of the selenide-dominated microparticles in the Ccp-Py and Py>Ccp zones, as epithermal fluids may also cause sericitization of silicate minerals (Arribas, Jr, 1995). However, the predominant association of hessite with bornite that formed >320°C and its lack of association with late sodic alteration suggests that exsolution is a more likely mechanism for formation of the telluride microparticles in the Ccp-Bn zone.

Another option is for a Bi-Te-Se melt to have separated directly from the hydrothermal fluid (Tooth et al., 2011), which could then have formed telluride and selenide minerals. Wagner and Wagner (2007) found that such a melt could form even from a fluid moderately undersaturated in both gold and Bi-Te. The lack of Bi-bearing minerals within sulphides in the Ccp-Bn zone make this unlikely to be a major mechanism for the deportment of precious metals at Ann Mason, but it is a possible explanation for the distribution of the distribution of Bi-minerals in the Py>Ccp zone and hosted by silicates within the Ccp-Bn zone. Evidence for this could include a multiphase microparticle of

562 hessite and Bi-telluride at the boundary between pyrite and chalcopyrite (Figure 7g), and that Bi-
563 tellurides are only present in the Ccp-Bn zone hosted by silicate minerals. Consistent with our
564 observation that Bi-tellurides are only observed in samples also containing high fineness native
565 gold, Zhou et al. (2021) show that an immiscible Bi-Au liquid crystallized native gold nanoparticles
566 in porous magnetite. However, the high fineness native gold microparticles in this study show no
567 close association with Bi-bearing minerals, so it seems more likely that they formed from the same
568 hydrothermal fluid, but likely without forming a Bi-Te-Se melt.
569 Since the high fineness native gold microparticle in the Ccp-Bn zone is hosted by silicate minerals
570 and the two in the Py>Ccp zone are hosted by pyrite, we propose that these three high fineness gold
571 particles represent a separate gold-forming event from the electrum, which is hosted dominantly in
572 bornite. Since gold is commonly transported as sulphide complexes under ore-forming conditions,
573 and silver is transported as Cl complexes, we suggest that the pyrite-forming event disrupted
574 sulphide complexes but left Cl complexes intact, causing separation of Ag from Au (e.g. Gregory et
575 al., 2013; Peng et al., 2021) and precipitating high fineness native gold with pyrite (Figure 9).
576

577 ## 6. Conclusions

578 This study shows that the precious and critical metals in the Ann Mason deposit are mostly present
579 as microparticles (<1 - 10μm) of electrum or Au-Ag telluride and selenide minerals, hosted by
580 bornite in the Ccp-Bn mineralization zone. Applications of these findings for industry include
581 informing the degree of milling (<10um) required for precious metal liberation and mitigating the
582 effects of the minor contaminants As and Hg that are present in the ores.
583 To summarise the formation of this deposit: chalcopyrite in the Ccp-Bn zone initially precipitated
584 from the hydromagmatic fluids released from the porphyry dykes, incorporating some Au and Ag
585 (Figure 8). During potassic alteration the fluids interacted with the chalcopyrite, converting it to
586 bornite around the edges and entirely replacing smaller crystals. The upgrade of chalcopyrite to

bornite allowed the bornite to incorporate additional precious and critical metals (Ag, Au, Te, Se, etc) into its crystal structure. During cooling, the chalcopyrite and bornite ripened and recrystallized, causing the fluid-mediated exsolution of microparticles and potentially some loss of some precious metals, Se and Te to the fluid. Some of the bornite also exsolved chalcopyrite lamellae.

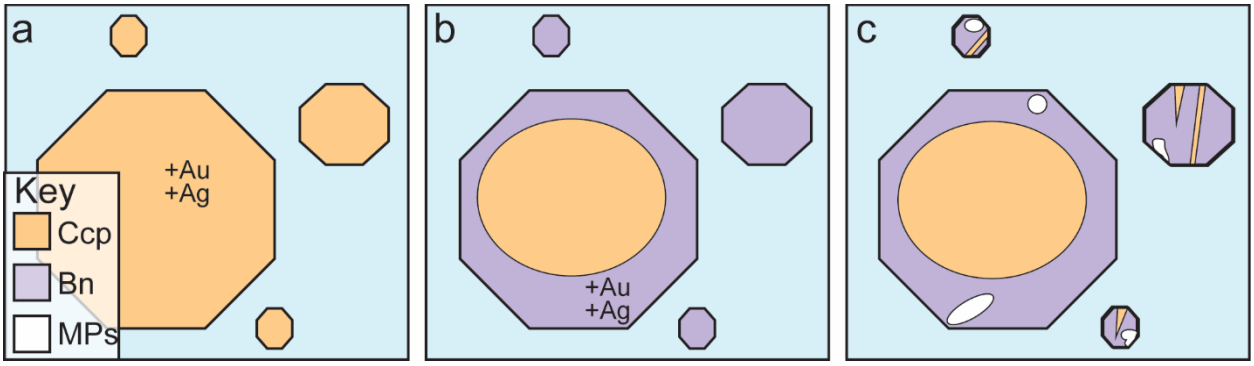

Figure 8: Schematic model of formation of the Ccp-Bn mineralization zone in the Ann Mason deposit. a) precipitation of chalcopyrite from hydrothermal fluid, including chalcophile precious metals; b) partial alteration of chalcopyrite to bornite through interaction with the fluid; c) cooling causes recrystallization of bornite producing exsolution of chalcopyrite lamellae and precious metal microparticles. Abbreviations: Ccp chalcopyrite, Bn bornite, MPs microparticles.

In the Ccp-Py and the Py>Ccp zones, low salinity, lower temperature fluids (Dilles and Einaudi, 1992) caused the precipitation of pyrite with chalcopyrite inclusions (Figure 9). Pyrite formation produced significant acid, hydrolysing the feldspars to sericite, and triggered deposition of sparse microparticles of minerals including high-fineness gold, electrum, hessite and Hg- and Bi-tellurides. Subsequent evolution of the fluid caused a new stage of Cu deposition, precipitating chalcopyrite along veins and around pyrite crystals.

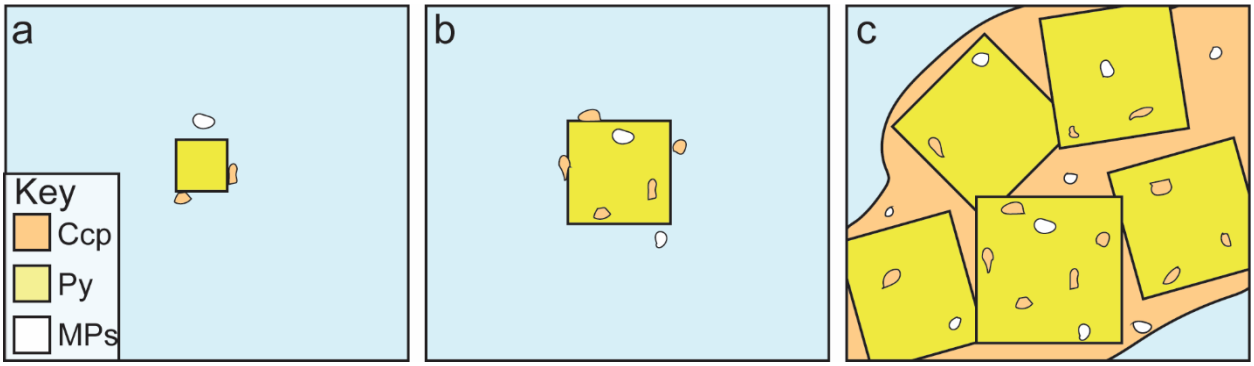

Figure 9: Schematic model of formation of the Ccp-Py and Py>ccp mineralization zones in the Ann Mason deposit. a) precipitation of euhedral pyrite and microparticles of chalcopyrite and precious metal minerals from the hydrothermal fluid; b) growth of pyrite, incorporating microparticles into pyrite; c) precipitation of chalcopyrite, enclosing pyrite. Abbreviations: Ccp chalcopyrite, Py Pyrite, MPs microparticles.

Author Contributions

CKP, NDW, JM, TC, JC, JB and ZM analysed the samples as their undergraduate research projects. HMA collected the samples, compiled the students' data, completed the analyses and wrote the paper.

Funding

This work was supported by a California State University, Chico Research, Scholarly and Creative Activity grant to HMA in 2016, as well as several departmental undergraduate research awards to CKP, NDW, JM and JB.

This research did not receive any specific grant from funding agencies in the public, commercial or not for profit sectors.

Acknowledgements

The authors thank Hudbay Minerals Inc. for samples and for permission to publish. We also thank UC Davis for access to the EPMA. The authors would like to acknowledge that our samples were

627 collected on the traditional lands of the Washoe and Northern Paiute people, and our analyses were
628 carried out at CSU Chico, which is on the traditional lands of the Mechoopda and Konkow people.

629

630 **References**

631 Agorhom, E.A., Skinner, W., Zanin, M., 2013. Influence of gold mineralogy on its flotation recovery in
632 a porphyry copper–gold ore. Chem. Eng. Sci. 99, 127–138.
633 https://doi.org/10.1016/j.ces.2013.05.037
634 Arif, J., Baker, T., 2004. Gold paragenesis and chemistry at Batu Hijau, Indoneisa: Implications for
635 gold-rich porphyry copper deposits. Miner. Deposita 39, 523–535.
636 https://doi.org/10.1007/s00126-004-0433-0
637 Arribas, Jr, A., 1995. Characteristics of high-sulfidation epithermal deposits, and their relation to
638 magmatic fluid. Mineral. Assoc. Can. Short Course 23, 419–454.
639 Ballantyne, G.H., Smith, T.W., Redmond, P.B., 1998. Distribution and Mineralogy of Gold and Silver in
640 the Bingham Canyon Porphyry Copper Deposit, Utah, in: John, D.A., Ballantyne, G.H. (Eds.),
641 Geology and Ore Deposits of the Oquirrh and Wasatch Mountains, Utah. Society of Economic
642 Geologists, p. 0. https://doi.org/10.5382/GB.29
643 Blundy, J., Mavrogenes, J., Tattitch, B., Sparks, S., Gilmer, A., 2015. Generation of porphyry copper
644 deposits by gas–brine reaction in volcanic arcs. Nat. Geosci. 8, 235–240.
645 https://doi.org/10.1038/ngeo2351
646 Brimhall, G.H., 1979. Lithologic determination of mass transfer mechanisms of multiple-stage
647 porphyry copper mineralization at Butte, Montana; vein formation by hypogene leaching
648 and enrichment of potassium-silicate protore. Econ. Geol. 74, 556–589.
649 https://doi.org/10.2113/gsecongeo.74.3.556
650 Carten, R.B., 1986. Sodium-calcium metasomatism; chemical, temporal, and spatial relationships at
651 the Yerington, Nevada, porphyry copper deposit. Econ. Geol. 81, 1495–1519.
652 https://doi.org/10.2113/gsecongeo.81.6.1495
653 Cioacă, M.-E., Munteanu, M., Lynch, E.P., Arvanitidis, N., Bergqvist, M., Costin, G., Ivanov, D., Milu, V.,
654 Arvidsson, R., Iorga-Pavel, A., Högdahl, K., Stoilov, V., 2020. Mineralogical Setting of Precious
655 Metals at the Assarel Porphyry Copper-Gold Deposit, Bulgaria, as Supporting Information
656 for the Development of New Drill Core 3D XCT-XRF Scanning Technology. Minerals 10, 946.
657 https://doi.org/10.3390/min10110946
658 Cook, N., Ciobanu, C., George, L., Zhu, Z.-Y., Wade, B., Ehrig, K., 2016. Trace Element Analysis of
659 Minerals in Magmatic-Hydrothermal Ores by Laser Ablation Inductively-Coupled Plasma
660 Mass Spectrometry: Approaches and Opportunities. Minerals 6, 111.
661 https://doi.org/10.3390/min6040111
662 Cook, N.J., Ciobanu, C.L., Danyushevsky, L.V., Gilbert, S., 2011. Minor and trace elements in bornite
663 and associated Cu-(Fe)-sulfides: A LA-ICP-MS study of bornite mineral chemistry. Geochim.
664 Cosmochim. Acta 75, 6473–6496. https://doi.org/10.1016/j.gca.2011.08.021
665 Crespo, J., Reich, M., Barra, F., Verdugo, J., Martínez, C., 2018. Critical Metal Particles in Copper
666 Sulfides from the Supergiant Río Blanco Porphyry Cu–Mo Deposit, Chile. Minerals 8, 519.
667 https://doi.org/10.3390/min8110519
668 Cuddy, A.S., Kesler, S., 1982. Gold in the Granisle and Bell copper porphyry copper deposits, British
669 Columbia., in: Precious Metals in the Northern Cordillera. Association or Exploration
670 Geochemists, Rexdale, Ontario, pp. 157–172.

671 Deditius, A.P., Utsunomiya, S., Reich, M., Kesler, S.E., Ewing, R.C., Hough, R., Walshe, J., 2011. Trace
672 metal nanoparticles in pyrite. Ore Geol. Rev. 42, 32–46.
673 https://doi.org/10.1016/j.oregeorev.2011.03.003
674 Dilles, J.H., 1987. Petrology of the Yerington Batholith, Nevada; evidence for evolution of porphyry
675 copper ore fluids. Econ. Geol. 82, 1750–1789.
676 https://doi.org/10.2113/gsecongeo.82.7.1750
677 Dilles, J.H., Einaudi, M.T., 1992. Wall-rock alteration and hydrothermal flow paths about the Ann-
678 Mason porphyry copper deposit, Nevada; a 6-km vertical reconstruction. Econ. Geol. 87,
679 1963–2001. https://doi.org/10.2113/gsecongeo.87.8.1963
680 Dilles, J.H., Solomon, G.C., Taylor, H.P., Einaudi, M.T., 1992. Oxygen and hydrogen isotope
681 characteristics of hydrothermal alteration at the Ann-Mason porphyry copper deposit,
682 Yerington, Nevada. Econ. Geol. 87, 44–63. https://doi.org/10.2113/gsecongeo.87.1.44
683 Gammons, C.H., Williams-Jones, A.E., 1997. Chemical mobility of gold in the porphyry-epithermal
684 environment. Econ. Geol. 92, 45–59. https://doi.org/10.2113/gsecongeo.92.1.45
685 Gammons, C.H., Williams-Jones, A.E., 1995. Hydrothermal geochemistry of electrum;
686 thermodynamic constraints. Econ. Geol. 90, 420–432.
687 https://doi.org/10.2113/gsecongeo.90.2.420
688 George, L.L., Cook, N.J., Crowe, B.B.P., Ciobanu, C.L., 2018. Trace elements in hydrothermal
689 chalcopyrite. Mineral. Mag. 82, 59–88. https://doi.org/10.1180/minmag.2017.081.021
690 Goldfarb, R.J., 2014. Tellurium: The Bright Future of Solar Energy. US Department of the Interior, US
691 Geological Survey.
692 Graham, U.M., Ohmoto, H., 1994. Experimental study of formation mechanisms of hydrothermal
693 pyrite. Geochim. Cosmochim. Acta 58, 2187–2202. https://doi.org/10.1016/0016-
694 7037(94)90004-3
695 Gregory, M.J., Lang, J.R., Gilbert, S., Hoal, K.O., 2013. Geometallurgy of the Pebble porphyry copper-
696 gold-molybdenum deposit, Alaska: Implications for gold distribution and paragenesis. Econ.
697 Geol. 108, 463–482. https://doi.org/10.2113/econgeo.108.3.463
698 Harris, D.C., 1990. The Mineralogy of gold and its relevance to gold recoveries. Miner. Deposita 25,
699 S3–S7. https://doi.org/10.1007/BF00205243
700 Hochella, M.F., Lower, S.K., Maurice, P.A., Penn, R.L., Sahai, N., Sparks, D.L., Twining, B.S., 2008.
701 Nanominerals, Mineral Nanoparticles, and Earth Systems. Science 319, 1631.
702 https://doi.org/10.1126/science.1141134
703 Johnson, K.M., Hammarstrom, J.M., Zientek, M.L., Dicken, C.L., 2014. Estimate of undiscovered
704 copper resources of the world. US Geol. Surv. Fact Sheet 3004.
705 Kesler, S.E., Chryssoulis, S.L., Simon, G., 2002. Gold in porphyry copper deposits: Its abundance and
706 fate. Ore Geol. Rev. 21, 103–124. https://doi.org/10.1016/S0169-1368(02)00084-7
707 Korges, M., Weis, P., Andersen, C., 2020. The role of incremental magma chamber growth on ore
708 formation in porphyry copper systems. Earth Planet. Sci. Lett. 552, 116584.
709 https://doi.org/10.1016/j.epsl.2020.116584
710 Li, K., Brugger, J., Pring, A., 2018. Exsolution of chalcopyrite from bornite-digenite solid solution: an
711 example of a fluid-driven back-replacement reaction. Miner. Deposita 53, 903–908.
712 https://doi.org/10.1007/s00126-018-0820-6
713 Li, K., Pring, A., Etschmann, B., Xia, F., Brugger, J., 2020. Coupling between mineral replacement
714 reactions and co-precipitation of trace elements: An example from the giant Olympic Dam
715 deposit. Ore Geol. Rev. 117, 103267. https://doi.org/10.1016/j.oregeorev.2019.103267
716 Pal'Yanova, G., Mikhlin, Y., Kokh, K., Karmanov, N., Seryotkin, Y., 2015. Experimental constraints on
717 gold and silver solubility in iron sulfides. J. Alloys Compd. 649, 67–75.
718 https://doi.org/10.1016/j.jallcom.2015.07.131
719 Palyanova, G.A., 2020. Gold and Silver Minerals in Sulfide Ore. Geol. Ore Depos. 62, 383–406.
720 https://doi.org/10.1134/S1075701520050050

721 Peng, H.-W., Fan, H.-R., Liu, X., Wen, B.-J., Zhang, Y.-W., Feng, K., 2021. New Insights Into the Control
722 of Visible Gold Fineness and Deposition: A Case Study of the Sanshandao Gold Deposit,
723 Jiaodong, China. Am. Mineral. 106, 135–149. https://doi.org/10.2138/am-2020-7475
724 Plotinskaya, O.Y., Azovskova, O.B., Abramov, S.S., Groznova, E.O., Novoselov, K.A., Seltmann, R.,
725 Spratt, J., 2018. Precious metals assemblages at the Mikheevskoe porphyry copper deposit
726 (South Urals, Russia) as proxies of epithermal overprinting. Ore Geol. Rev. 94, 239–260.
727 https://doi.org/10.1016/j.oregeorev.2018.01.025
728 Pokrovski, G.S., Borisova, A.Yu., Harrichoury, J.-C., 2008. The effect of sulfur on vapor–liquid
729 fractionation of metals in hydrothermal systems. Earth Planet. Sci. Lett. 266, 345–362.
730 https://doi.org/10.1016/j.epsl.2007.11.023
731 Proffett, J.M. and Dilles, J.H., 1984. Geologic map of the Yerington district, Nevada.
732 Proffett, J.M., 2007. Report on the Geology and Genesis of the Yerington Porphyry Copper District,
733 Nevada, A Four Dimensional Study. As supported by USGS Mineral Resource External
734 Research Program Grant 06HQGR0171 (USGS Mineral Resource External Research Program
735 Grant 06HQGR0171).
736 Rees, C., Riedell, K.B., Proffett, J.M., Macpherson, J., Robertson, S., 2015. The Red Chris porphyry
737 copper-gold deposit, northern British Columbia, Canada: Igneous phases, alteration, and
738 controls of mineralization. Econ. Geol. 110, 857–888.
739 https://doi.org/10.2113/econgeo.110.4.857
740 Reich, M., Palacios, C., Barra, F., Chryssoulis, S., 2013. “Invisible” silver in chalcopyrite and bornite
741 from the Mantos Blancos Cu deposit, northern Chile. Eur. J. Mineral. 25, 453–460.
742 https://doi.org/10.1127/0935-1221/2013/0025-2287
743 Reich, M., Román, N., Barra, F., Morata, D., 2020. Silver-Rich Chalcopyrite from the Active Cerro
744 Pabellón Geothermal System, Northern Chile. Minerals 10, 113.
745 https://doi.org/10.3390/min10020113
746 Rubin, J.N., Kyle, J.R., 1997. Precious metal mineralogy in porphyry-, skarn-, and replacement-type
747 ore deposits of the ertsberg (Gunung Bijih) district, Irian Jaya, Indonesia. Econ. Geol. 92,
748 535–550. https://doi.org/10.2113/gsecongeo.92.5.535
749 Ruiz-Agudo, E., Putnis, C.V., Putnis, A., 2014. Coupled dissolution and precipitation at mineral–fluid
750 interfaces. Chem. Geol. 383, 132–146. https://doi.org/10.1016/j.chemgeo.2014.06.007
751 Schulz, K.J., DeYoung, J.H., Seal, R.R., Bradley, D.C., 2018. Critical mineral resources of the United
752 States: economic and environmental geology and prospects for future supply. Geological
753 Survey.
754 Simon, G., Kesler, S.E., Essene, E.J., 2000. Gold in Porphyry Copper Deposits: Experimental
755 Determination of the Distribution of Gold in the Cu-Fe-S System at 400° to 700°C. Econ.
756 Geol. 95, 259–270.
757 Steadman, J.A., Large, R.R., Olin, P.H., Danyushevsky, L.V., Meffre, S., Huston, D., Fabris, A., Lisitsin, V.,
758 Wells, T., 2021. Pyrite trace element behavior in magmatic-hydrothermal environments: An
759 LA-ICPMS imaging study. Ore Geol. Rev. 128, 103878.
760 https://doi.org/10.1016/j.oregeorev.2020.103878
761 Suerte, L.O., Nishihara, S., Imai, A., Watanabe, K., Yumul, G.P., Maglambayan, V.B., 2007. Occurrences
762 of ore minerals and fluid inclusion study on the Kingking Porphyry copper-gold deposit,
763 Eastern Mindanao, Philippines, in: Resource Geology. pp. 219–229.
764 https://doi.org/10.1111/j.1751-3928.2007.00018.x
765 Sugaki, A., Kitakaze, A., Hayashi, K., 1984. Hydrothermal synthesis and phase relations of the
766 polymetallic sulphide system, especially on the Cu-Fe-Bi-S system. Mater. Sci. Earths Inter.
767 545–583.
768 Tarkian, M., Koopmann, G., 1995. Platinum-group minerals in the Santo Tomas II (Philex) porphyry
769 copper-gold deposit, Luzon Island, Philippines. Miner. Deposita 30, 39–47.

770 Tooth, B., Ciobanu, C.L., Green, L., O'Neill, B., Brugger, J., 2011. Bi-melt formation and gold
771 scavenging from hydrothermal fluids: An experimental study. Geochim. Cosmochim. Acta
772 75, 5423–5443. https://doi.org/10.1016/j.gca.2011.07.020
773 Tungpalan, K., Wightman, E., Manlapig, E., 2015. Relating mineralogical and textural characteristics
774 to flotation behaviour. Miner. Eng. 82, 136–140.
775 https://doi.org/10.1016/j.mineng.2015.02.005
776 Wagner, T., 2007. Thermodynamic modeling of Au-Bi-Te melt precipitation from high-temperature
777 hydrothermal fluids: Preliminary results, in: Proceedings of the Ninth Biennial SGA Meeting,
778 Dublin. Presented at the SGA, Dublin.
779 Williams-Jones, A.E., Heinrich, C.A., 2005. 100th Anniversary Special Paper: Vapor Transport of
780 Metals and the Formation of Magmatic-Hydrothermal Ore Deposits. Econ. Geol. 100, 1287–
781 1312. https://doi.org/10.2113/gsecongeo.100.7.1287
782 Zhang, Y., Cai, Y., Qu, Y., Wang, Q., Gu, L., Li, G., 2020. Two-stage fluid pathways generated by volume
783 expansion reactions: insights from the replacement of pyrite by chalcopyrite. Sci. Rep. 10,
784 19993. https://doi.org/10.1038/s41598-020-76813-9
785 Zhao, J., Brugger, J., Grguric, B.A., Ngothai, Y., Pring, A., 2017. Fluid-Enhanced Coarsening of Mineral
786 Microstructures in Hydrothermally Synthesized Bornite-Digenite Solid Solution. ACS Earth
787 Space Chem. 1, 456–474. https://doi.org/10.1021/acsearthspacechem.7b00034
788 Zhao, J., Brugger, J., Ngothai, Y., Pring, A., 2014. The replacement of chalcopyrite by bornite under
789 hydrothermal conditions. Am. Mineral. 99, 2389–2397. https://doi.org/10.2138/am-2014-
790 4825
791 Zhao, J., Pring, A., 2019. Mineral Transformations in Gold–(Silver) Tellurides in the Presence of
792 Fluids: Nature and Experiment. Minerals 9, 167. https://doi.org/10.3390/min9030167
793 Zhou, H., Wirth, R., Gleeson, S.A., Schreiber, A., Mayanna, S., 2021. Three-Dimensional and
794 Microstructural Fingerprinting of Gold Nanoparticles at Fluid-Mineral Interfaces. Am.
795 Mineral. 106, 97–104. https://doi.org/10.2138/am-2021-7696
796